

# **Electron Acceleration from Expanding Magnetic Vortices During Reconnection with a Guide Field**

H. Che<sup>1,2</sup> and G. P. Zank<sup>1,2</sup>

Center for Space Plasma and Aeronomic Research (CSPAR), University of Alabama in Huntsville, Huntsville, AL 35805, USA; hc0043@uah.edu
Department of Space Science, University of Alabama in Huntsville, Huntsville, AL 35899, USA
Received 2019 August 27; revised 2019 November 14; accepted 2019 November 26; published 2020 January 20

### **Abstract**

Magnetic reconnection is believed to be responsible for the acceleration of energetic electrons with a power-law spectrum in the solar wind and solar flares. However, recent studies of the leading mechanism of electron acceleration in reconnection, namely the acceleration by tearing instability induced multi-islands, demonstrates that this mechanism suffers from an "injection problem" for mildly relativistic reconnection acceleration. In this paper, we investigate a new type of reconnection acceleration in which an electron Kelvin–Helmholtz instability (EKHI) is driven as the current sheet reaches electron inertial length scales during magnetic reconnection with a strong guide field. Electrons are accelerated by stochastic electric fields, induced by the EKHI generated vortices that expand rapidly, and a power-law electron energy spectrum  $f(W) \propto W^{-\alpha}$  with index  $\alpha \sim 3.5$  is produced (W is the electron kinetic energy and f(W) is the energy distribution function). We show that the mechanism is a second-order Fermi acceleration process, and the index  $\alpha = (1 + 4a^2D/R)/2$  where  $a = B_g/B_0$ , which is determined by the ratio of the spatial scale of the inductive electric field D to that of vortices R and the ratio of guide field  $B_g$  to asymptotic magnetic field  $B_0$ .

Unified Astronomy Thesaurus concepts: Solar energetic particles (1491); Solar magnetic reconnection (1504); Solar flares (1496)

Supporting material: animation

#### 1. Introduction

Magnetic reconnection (MR) is believed to play a central role in charged particle energization in explosive events observed in nature: for example, magnetospheric substorms (e.g., Dungey 1961; Galeev et al. 1986; Baker et al. 1996; Zelenyi et al. 2010), solar wind turbulence (e.g., Gosling & Phan 2013; Zank et al. 2014, 2015; Vech et al. 2018), solar flares (e.g., Lin 2011; Benz 2017),  $\gamma$ -ray flares in the pulsar nebulae (e.g., Tavani et al. 2011; Bühler & Blandford 2014; Blandford et al. 2017), and  $\gamma$ -ray bursts (e.g., Kouveliotou et al. 2012; Blandford et al. 2017). However, how MR produces an inverse power-law energy spectra  $f(W) \propto W^{-\alpha}$  ( $W \equiv mv^2/2$  is the particle kinetic energy) ubiquitous to the observed energetic particles is still poorly understood (Gloeckler et al. 2000; Stone et al. 2005; Lin 2011; Blandford et al. 2014).

For energetic electrons, first-order Fermi acceleration from contracting magnetic islands generated by a tearing instability has emerged as a leading mechanism (Kliem 1994; Drake et al. 2006; Lin 2011). In this scenario, the particles gain energy as they move around the contracting magnetic islands and escape the confinement of the magnetic islands by curvature drift acceleration (Kliem 1994; Drake et al. 2006; Zank et al. 2014; le Roux et al. 2018). Before escaping from the acceleration region, the particles experience multiple accelerations by randomly distributed islands and stochastic scattering. The stochastic motion is caused by magnetic fluctuations induced by the merging of the islands, resulting in a power-law energy distribution (Drake et al. 2013; Zank et al. 2014; le Roux et al. 2015). Numerical studies, however, seem to suggest that the mechanism has an "injection problem" (Oka et al. 2010; Drake et al. 2013; Dahlin et al. 2014, 2017; Guo et al. 2014, 2016; Sironi & Spitkovsky 2014; Werner et al. 2016; Muñoz & Büchner 2018). Using particle-in-cell (PIC) simulations, Guo

et al. (2014, 2016) showed that in highly relativistic (a Lorentz factor  $\gamma \gtrsim 100$ ) and highly magnetized plasma ( $\Omega_{ce}^2/\omega_{pe}^2 \gtrsim 1$ and up to 10<sup>5</sup>), the electrons can be accelerated to a power-law energy distribution with an index  $\alpha$  < 2, while Dahlin et al. (2014, 2017) and Huang et al. (2015, 2017) found that in mildly relativistic reconnection, PIC simulations fail to produce a power-law energy distribution even though the plasma turbulent heating is strong. It was found that a power law is produced only at the x-line of the reconnection (Muñoz & Büchner 2018). However, the analytical study (Zank et al. 2014) show that a power-law velocity distribution with index  $3(1 + \tau_c/8\tau_{diff})$ , or an energy spectrum  $\alpha = 3(1 + \tau_c/8\tau_{\rm diff})/2$  (see Section 3) is guaranteed as long as the adiabatic invariants and random motions are assumed. The underlying assumption of Zank et al. (2014) that decides the power-law distribution is that the charged particles are sufficient to diffuse throughout the multi-island acceleration region before escaping, thus introducing an "injection problem" as seen in simulations of mildly relativistic reconnection. In such reconnections particles may not interact with enough number of islands and attain sufficient randomness, as the particles are confined in the islands for too long due to the mirror effect, and  $\tau_{\text{diff}}$  is too large (Che & Zank 2019).

Particle acceleration in solar flares and the solar wind remains unsolved due to the injection problem. The Lorentz factor  $\gamma$  of energetic electrons in solar flares is usually less than 2. Above a few tens keV, the electrons have power-law spectra with indices >3 (Lin 2011; Benz 2017; Oka et al. 2018), which is softer than the electron spectra seen in multi-island MR simulations. In addition, the acceleration in solar flares is very efficient. Hard X-ray observations (Kiplinger et al. 1984) imply that the electron kinetic energy increases by about two orders of magnitude in less a second. This timescale is a tiny fraction of

the duration of solar flares. If the duration of MR is comparable with that of solar flares, these observations imply that a more efficient reconnection acceleration mechanism is common in solar flares that produce the observed power-law energy spectrum. In this paper, we report a new two-phase electron acceleration mechanism. Electrons are accelerated by the fast growing multivortices generated by an electron Kelvin-Helmholtz instability (EKHI) during MR with a strong guide field. We show that the EKHI efficiently twists and entangles the antiparallel magnetic field lines and generates stochastically distributed and localized inductive electric fields inside the vortices. In the linear phase of the EKHI (first phase), the random electric fields accelerate electrons to a power-law energy distribution with  $\alpha \sim 7.5$ ; In the nonlinear phase (second phase), the electrons are continuously accelerated and achieve a power law with  $\alpha \sim 3.5$ . A simple analysis shows that the mechanism is a second-order Fermi acceleration, and the mean index of the power-law energy spectrum is  $\alpha = (1 + 4a^2D/R)/2$ , where D is the mean spatial scale of the random inductive electric field, R is the mean size of the vortices, and  $a = B_g/B_0$  is the ratio of guide field  $B_g$  to asymptotic magnetic field  $B_0$ . The power-law index  $\alpha$ decreases with the expanding vortices and  $\alpha \sim 3.5$  at the saturation of EKHI with D/R = 1/4 and a = 2.5.

### 2. Simulation Setup and Results

Three dimensional PIC simulations using the p3d code are carried out in doubly periodic geometry starting with double force-free current sheets and a strong guide field. The initial reconnection magnetic field is  $B_x/B_0 = \tanh[(y - L_y/2)/w_0]$ , where  $B_0$  is the asymptotic amplitude of  $B_x$ ,  $w_0$  is the half-width of the initial current sheet, and  $L_y$  is the domain size in the y direction. The guide field  $B_g^2 = B^2 - B_x^2$  is chosen so that the total field B is constant and guide field is in z-direction  $B_g = B_z \hat{z}$ . In our simulation, we have adopted  $w_0 = 0.5d_i$  and  $B^2 = 7.25B_0^2$ , where  $d_i = c/\omega_{pi}$  and  $\omega_{pi}$  is the ion plasma frequency. The initial temperatures satisfy  $T_{e0} = T_{i0}$  and  $\beta = 0.04$ . The mass ratio is  $m_i/m_e = 100$ . The ratio of electron plasma frequency  $\omega_{pe}$  to electron gyrofrequency is 2. The domain has dimensions  $L_x \times L_y \times L_z = 64d_i \times 16d_i \times 0.25d_i$  with grid number  $8192 \times 2048 \times 32$ . The very shallow simulation box suppresses the growth of other instabilities in the z-direction and allows only EKHI to fully develop so that the physics of particle acceleration by vortices can be better demonstrated compared to the 2D simulation. The physical results from 2D are similar to 3D, thus we do not show 2D simulation in this paper. The particle number per cell is 100. In the simulation, the temperature is normalized to  $m_i v_{A0}^2$  ( $v_{A0} = B_0/(4\pi n_0 m_i)^{1/2}$ is the asymptotic ion Alfvén wave speed), mass is normalized to  $m_i$ , density to the asymptotic density  $n_0$ , the magnetic field to  $B_0$ , and the electric field to  $E_0 = v_{A0}B_0/c$ . The MR is initialized to produce a primary x-line at  $x = L_x/4 = 16d_i$ and an island centered at  $x = 3L_x/4 = 48d_i$ . The total simulation time is  $\Omega_i t = 35$ , where  $\Omega_i$  is the ion gyrofrequency.

As MR proceeds, the current sheet gradually develops a primary x-line with the maximum current density  $j_{ez}$  and a magnetic island centered at the minimum  $j_{ez}$  (Figure 1). Around  $\Omega_i t \sim 15$ , the intensive current  $j_{ez}$  at the x-line shrinks to  $d_e$  and an EKHI is triggered. As shown in Figure 1, around  $\Omega_i t \sim 23$ , vortices with spatial scale  $d_e$  develop around the x-line. The vortices continuously expand while new vortices are born.

Around  $\Omega_i t \sim 30.5$  the size of the oldest vortices increases to  $2d_i$ . The primary magnetic island continues to develop as the MR proceeds as is shown in Figure 1 (see its accompanying animation). The EKHI efficiently dissipates magnetic energy and accelerates the MR process. Around  $\Omega_i t \sim 34.5$ , both MR and the EKHI nearly saturate.

The EKHI is driven by the antiparallel electron flow developed during MR in the x-direction, and is an electromagnetic instability. We show  $|v_{ex}| - |v_{Aex}|$  at  $\Omega_i t = 23.9$  in Figure 2, where  $v_{Aex} = B_x/(4\pi n_e m_e)^{1/2}$  is the local electron Alfvén wave speed. We can see that  $|v_{ex}| - |v_{Aex}|$  is generally greater than zero inside the left side of the current sheet, and the velocity difference peaks correspond to the locations of vortices. The characteristic linear growth rate of EKHI is  $\gamma \sim \Delta v_{ex}/\Delta$ , where  $\Delta$  is the width of the current sheet and  $\Delta \sim d_e$ . We estimate the linear growth rate inside the vortices as  $\gamma \sim v_{Ae}/d_e \sim \Omega_e$ , where  $\Omega_e = eB/(m_e c)$  is the electron gyrofrequency. Thus EKHI is much faster than the tearing instability whose growth rate is  $\sim \Omega_i$  (Daughton et al. 2011). The EKHI quickly passes its linear stage and enters a nonlinear evolution stage, which lasts about  $10 \Omega_i^{-1}$ . The kinetic turbulence generated by the EKHI on electron inertial length scales quickly transfers the magnetic energy from an electron dynamic scale to an ion dynamic scale with the evolving vortices. We show around the linear stage ( $\Omega_i t \sim 20$ ) that the magnetic fluctuations have a power-law magnetic power spectrum  $|B(k_x)^2| \sim k^{-1.5}$ , and when the EKHI enters the nonlinear stage, the spectrum quickly evolves  $|B(k_x)^2| \sim k^{-2.7}$  around  $\Omega_i t = 23.9$ , and saturates due to the expansion of vortices or inverse energy transfer (Figure 3). The power-law magnetic energy spectrum indicates that the kinetic turbulence associated with vortices is fully developed around the time.

The vortices that develop within the current sheet are similar to typical KHI vortices generated by antiparallel flow. During the evolution of the EKHI, the vortices expand and interact with each other, accompanied by a mixture of electron flows. The velocity shear leads to the circulating movement of the current, and the twist and entanglement of antiparallel magnetic fields, resulting in localized MR and efficient dissipation of the magnetic energy. The electron velocity and magnetic field in the x-y plane at  $\Omega_i t \sim 30.5$  are shown in Figure 4. Different from electrons in MR magnetic islands, which flow along the separatrices, the plot of the electron velocity fields show that the electrons circulate along the magnetic vortices. The magnetic vector field shows that multiple x-lines are formed between the vortices. These new small-scale MRs dominate the release of magnetic energy and the primary x-line of the reconnection drift from the initial location  $x = 16d_i - 30d_i$ , where it connects to the primary magnetic island (see Figure 1).

During the expansion of magnetic vortices, the magnetic energy inside the vortices is released. Assuming that the magnetic flux inside the vortices is conserved during the expansion, i.e.,  $B_xR \sim \text{constant}$ , then  $B_0R_0 \sim B_{xt}R_t$ , where the subscript t represents R or  $B_x$  at time t. The typical size of the vortices increases from  $d_e$  to  $d_i$ , hence the change of  $B_x$  at the saturation of EKHI is about  $B_{xt} \sim B_0/10$  (we used  $d_i/d_e = (m_i/m_e)^{1/2} \sim 10$ ), which is consistent with the magnetic field in the vortices  $B_x/B_0 \sim 0.1$ , as shown in Figure 4(b). As a result, the regions outside the vortices accumulate magnetic energy due to the pile-up of magnetic

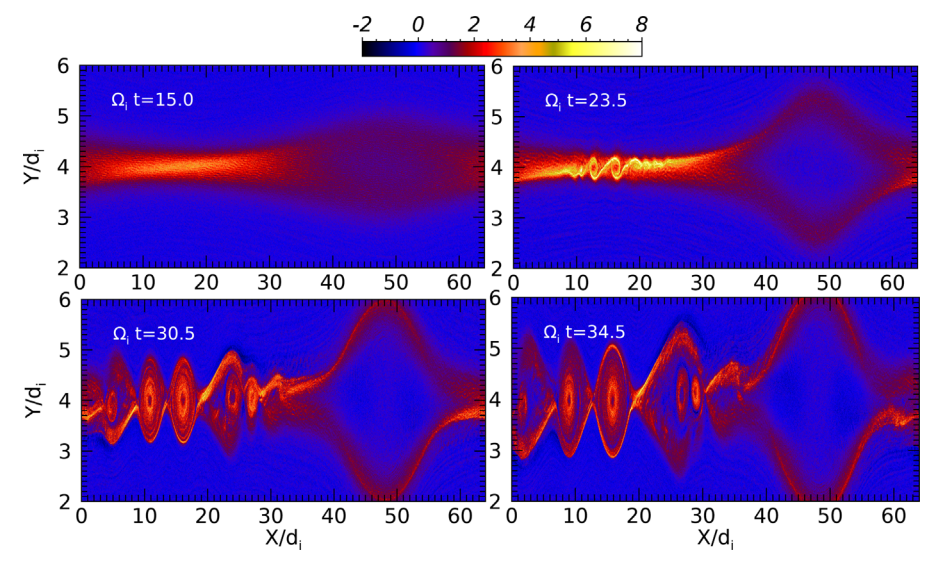
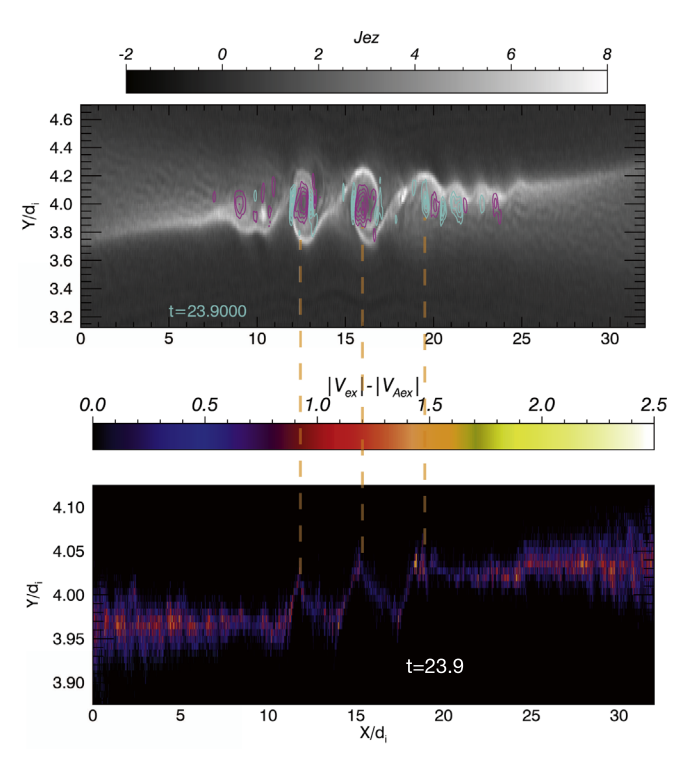


Figure 1.  $j_{ez}$  in the top half of the simulation domain. Vortices, the x-line and the reconnection island are shown. The video begins at  $\Omega_i t = 15$  and ends at  $\Omega_i t = 34.5$  and has a real-time duration of 7 s. The movie demonstrates how the vortices develop and expand during the evolution of EKHI. (An animation of this figure is available.)



**Figure 2.** Top: the grayscale image shows the  $j_{ez}$  at  $\Omega_i t = 23.9$  overlaid with electric field  $E_z$  contours. The electric field is induced by the expansion of vortices. The pink and cyan contours represent positive and negative electric field. Bottom:  $|v_{ex} - v_{Aex}|$  at  $\Omega_i t = 23.9$ . The peaks correspond to the strongest vortices in the top panel. Note that the two panel use different spatial scales in the y direction for better visualization.

field lines caused by the expansion of vortices (also see the Figure 1 animation).

The fast decrease of magnetic field inside the magnetic vortices leads to the generation of an inductive electric field through Faraday's law  $c\nabla \times E = -\partial B/\partial t$ . From the simulation, the magnetic field changes  $\delta B \sim B_0$  within  $\sim \Omega_i^{-1}$ , and the estimated inductive electric field is  $\sim E_z/E_0 \sim R/d_i \sim 2$ , which agrees with the inductive  $E_z$  obtained in the simulations

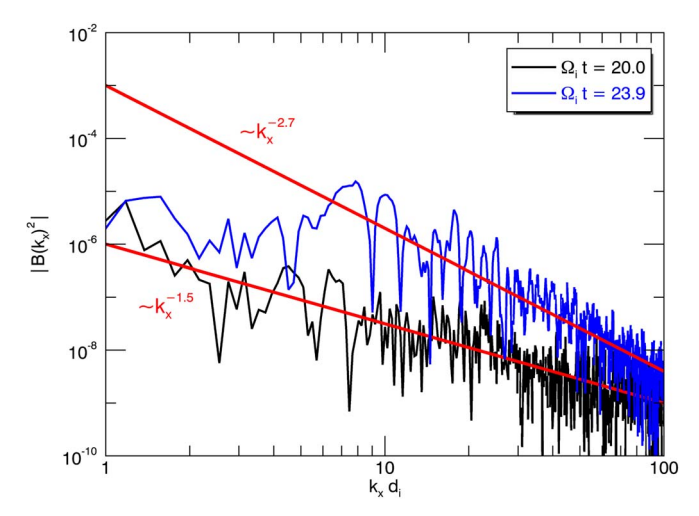


**Figure 3.** Power spectrum of magnetic fluctuations inside the vortices at  $\Omega_t = 20$  and  $\Omega_t = 23.9$ .

as shown in Figure 6. The direction of the inductive  $E_z$  changes stochastically inside the vortices, the spatial scales of the localized  $E_z$  in the x-y plane are determined by the magnetic fluctuations generated by EKHI and are randomly distributed. The mean  $E_z$  over the vortices is non-zero, which eventually accelerates particles and converts the magnetic energy into kinetic energy.

The inductive  $E_z$  generated by magnetic turbulence leads to the stochastic acceleration of electrons. To demonstrate how stochastic fields accelerate electrons, we performed a series of test particle simulations with different initial positions and velocities using the electric and magnetic fields extracted from the simulation at  $\Omega_i t = 23.9$ , a moment during the nonlinear growth of EKHI. The velocity component in the z-direction  $v_z$  of these test electrons increases and decreases due to the negative and positive variation in  $E_z$ , and these electrons gradually spiral out of the vortices along magnetic field lines due to the drift in the x-y plane perpendicular to the magnetic field  $v_d = E_z \hat{z} \times B/B^2$ . On average, electrons are accelerated along the z-direction. The velocities of these test electrons in x

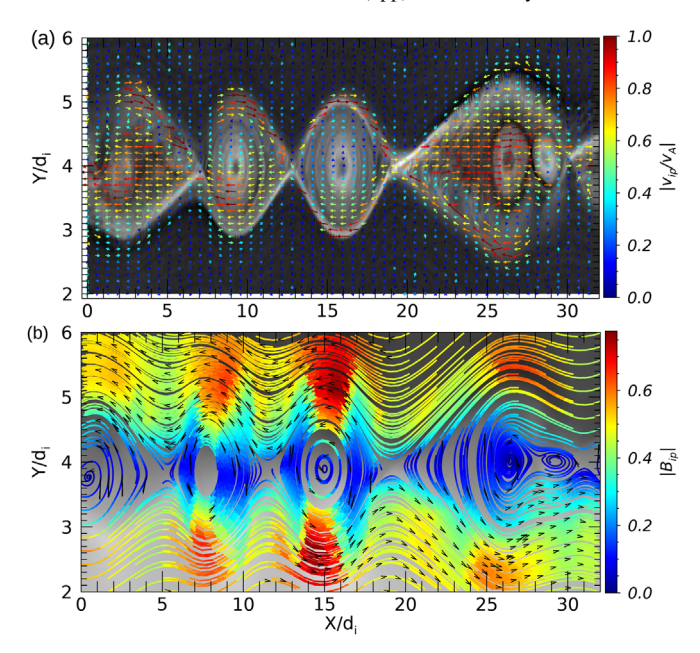


**Figure 4.** Corresponding velocity vector field (panel (a)) and magnetic vector field (panel (b)) in the current sheet at  $\Omega_i t = 30.5$ .

and y directions commonly show high-frequency oscillations between negative and positive, and the mean is close to zero. The test particle simulations show that electrons can escape the vortex within about a few ion gyroperiods due to  $v_d$  drift, comparable with the nonlinear growth timescale of EKHI. The long stay inside the vortices enables the electron motion to fully randomize. These are the common characteristics of the acceleration produced by the stochastic inductive  $E_z$ . The escaped electrons can be scattered among the vortices and be reaccelerated by other vortices.

We show the trajectory of a test electron plotted on top of  $j_{ez}$  and the corresponding  $E_z$  at  $\Omega_i t = 23.9$  in Figure 5. The test electron drifts out of the vortex and then drifts back to the edge, and experiences both positive and negative  $E_z$  along its trajectory. When the test electron moves to the edge of the vortex, it is accelerated steadily by a negative  $E_z$ . We also plot the time evolution of  $\log W/W_0$  and  $v_{ex}, v_{ey}$  and  $v_{ez}$  normalized to  $v_A$  in Figure 5, where  $W_0$  and  $v_A$  are the initial kinetic energy and Alfvén speed respectively. We see that  $\log W/W_0$  oscillates near zero before  $\Omega_i t = 2.0$  and then continuously increases. From the plot of  $v_{x,y,z}/v_A$ , the acceleration of  $v_z$  is primarily responsible for the increase of the electron kinetic energy.

The inductive electric fields generated during the expansion of vortices at different times are shown in Figure 6. A nonnegligible inductive  $E_z$  is generated around  $\Omega_i t \sim 20$  when the EKHI enters its nonlinear evolution stage (at  $\Omega_i t \sim 15$ ,  $E_z$  is too weak and is not shown here). Then, with the fast nonlinear growth of the EKHI, the inductive  $E_z$  increases to peak near  $\Omega_i t \sim 22.5$  and begins to decay after  $\Omega_i t \sim 25$ . Thus, the most efficient acceleration occurs between  $\Omega_i t \sim 20$  and 25. For comparison, in Figure 6 we also show both the electron energy and velocity distribution functions inside the vortices (solid lines) and the primary magnetic island (dashed lines) at different times. The electron energy distribution functions inside the vortices show an obvious two-phase acceleration, which is consistent with the development of the inductive  $E_z$ . The acceleration starts near  $\Omega_i t \sim 15$  when the EKHI is at the linear stage, and the tail of the corresponding energy distribution function starts to harden and becomes a power law at  $\Omega_i t \sim 20$  with  $f(W) \sim W^{-7.5}$  (solid brown line). The acceleration then enters the second phase as the EKHI becomes nonlinear, and particle acceleration becomes much more efficient than during the linear stage. The power-law energy index reaches -3.5 at  $\Omega_i t \sim 25$  when the kinetic turbulence saturates (solid orange line). After that, the electrons are only slightly accelerated. The kinetic energy of electrons increases to a 10-100 times larger than the initial electron thermal energy, and the fraction of accelerated electrons above 10  $m_e v_{le0}^2$  over the background in the vortices reaches about 10% while the fraction in the magnetic island is about 4%.

As a comparison, in Figure 6 we find that the electron energy spectrum inside the primary magnetic island hardens continuously, but does not fully develop into a power law at  $\Omega_i t \sim 35$  (purple dashed line). The spectrum is also lower than the spectrum from the vortices, demonstrating that the acceleration by the contraction of the magnetic island is less efficient than the acceleration by vortex expansion, and the electrons inside the magnetic island do not experience the same kind of stochastic acceleration to generate a power law. Note that the accelerated electrons in the vortices can flow into the magnetic island, and contribute to the observed spectrum in the island, and the actual difference between acceleration by vortex expansion and magnetic island contraction should be larger.

The velocity distribution functions  $f(v_x)$ ,  $f(v_y)$  and  $f(v_z)$  at  $\Omega_i t \sim 35$  (solid lines) show that  $f(v_z)$  (green line) has a significantly hotter tail than  $f(v_x)$  and  $f(v_y)$ , indicating that the acceleration is dominated by  $E_z$  and the acceleration is anisotropic. On the other hand, the velocity distribution functions obtained from the primary magnetic island do not show such anisotropy.

# 3. Acceleration by Stochastic Electric Fields Induced by the Expansion of Vortices

The EKHI grows in the reconnection plane (xy plane), and the expansion of turbulent vortices induces randomly localized electric fields in the z-direction  $E_z$ . The growth time of vortices is  $\tau_g \gg \Omega_e^{-1}$ . The acceleration by turbulent  $E_z$  produces a power-law velocity/energy distribution. Let  $\mathbf{B} = \mathbf{B}_{ip} + B_z \hat{z}$ , where  $\mathbf{B}_{ip} = B_x \hat{x} + B_y \hat{y}$  (the subscript ip denotes the in-plane components). We define  $\hat{b} \equiv \mathbf{B}/B$ ,  $\hat{b}_{ip} \equiv \mathbf{B}_{ip}/B_{ip}$ , and  $\cos \theta = \hat{b} \cdot \hat{b}_{ip}$ .

According to Faraday's Law, we have

$$\oint E_z \hat{z} \cdot d\mathbf{l} = -\frac{1}{c} \int_{\mathbf{S}} \frac{\partial \mathbf{B}_{ip}}{\partial t} \cdot d\mathbf{S}, \tag{1}$$

where the integration loop is along a random electron's gyroorbit whose orbit plane is perpendicular to the magnetic field. Both the first and second adiabatic invariants are no longer preserved, due to the presence of  $E_7$ .

The equation of the motion of an electron is

$$m_e \frac{dv_z}{dt} \hat{z} = -eE_z \hat{z}, \qquad (2)$$

where the acceleration in the z-direction from the second term  $\mathbf{v} \times \mathbf{B}/c$  is negligible, because  $\hat{b}$  is nearly parallel to  $\hat{z}$  and  $\hat{b} \times \hat{z} = \cos \theta \ll 1$ .

The Faraday's law  $\nabla \times \mathbf{E} = 1/c\partial \mathbf{B}_{ip}/\partial t$  and Equation (2) imply that the electrons gain energy due to  $E_z$  during the

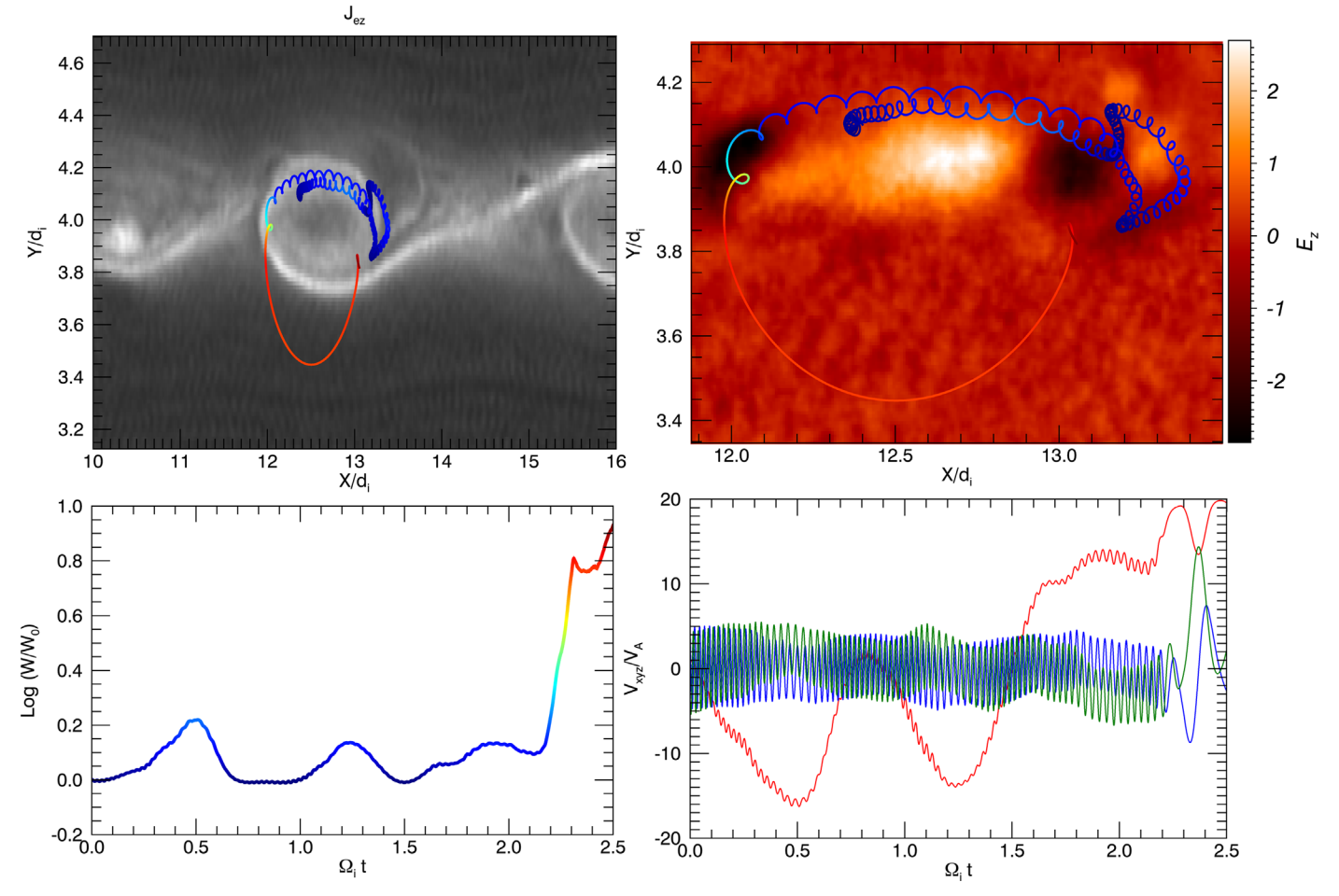


Figure 5. Example of test particle simulations at  $\Omega_i t = 23.9$ . The trajectories are plotted over the current density  $j_{ez}$  and electric field  $E_z$  respectively in the top left and right panels. The time evolution of test electron energy  $\log(W/W_0)$  and test electron velocity components  $v_{ex}/v_A$  (green),  $v_{ey}/v_A$  (blue) and  $v_{ez}/v_A$  (red) are shown in the bottom panels. The colors match the trajectory plots correspond to the kinetic energy  $\log(W/W_0)$ .

gyromotion around the magnetic field, and the gyrofrequency is  $\Omega_e$ . The gyroradius  $r_L$  is related to the gyrospeed  $v_L \hat{\perp}$ , where  $\hat{\perp}$  is the direction perpendicular to the magnetic field  $\hat{b}$ , by  $v_L = r_L \Omega_e$ . The gyroperiod is  $T = 2\pi \Omega_e^{-1}$ . Multiply Equation (2) by  $v_L \hat{\perp}$  on both sides and integrate Equation(2) over one gyroperiod T, to obtain

$$v_L \cos \theta \int_T dv_z = -\frac{e}{m_a} \int_T E_z \hat{z} \cdot v_L \, \hat{\perp} \, dt, \tag{3}$$

where  $\hat{z} \cdot \hat{\perp} = \cos \theta$ . Let the change of  $v_z$  in one gyroperiod T be  $\delta v_z$  and  $v_L T = 2\pi r_L$ . Then from Equations (3) and (1), we have

$$v_L \delta v_z = \frac{e}{m_e c} \frac{\partial B_{ip}}{\partial t} \pi r_L^2, \tag{4}$$

where  $\partial B_{ip}/\partial t$  is treated as a constant during the gyroperiod T due to the growth time of vortices  $\tau_g \gg \Omega_e^{-1}$ .

As we approximate  $\partial B_{ip}/\partial t \sim B_{ip}/\tau_g$ , the mean acceleration rate of  $v_z$  over one gyroperiod  $\delta t = T$  is then

$$\frac{\delta v_z}{\delta t} = \frac{\cos^2 \theta}{2\tau_g} v_z = \frac{F_z}{m_e},\tag{5}$$

where we used  $v_L \approx v_z \cos \theta$ , and ignored the contribution from  $v_{ip}$  because of  $v_{ip} \ll v_z$ . As  $v_z \to c$ , approximate

 $\cos^2 \theta \sim (v_L/c)^2 \ll 1$ , indicating that this is a second-order Fermi acceleration process.

As the acceleration is primarily in the z-direction, we neglect the acceleration in the x and y directions. The diffusion of electrons, on the other hand, is primarily in the x and y directions due to scattering by magnetic turbulence generated by the EKHI. f is approximately independent of z. Assume  $f = f_x f_y f_z(x, y, v_z)$ , where  $f_x = (m_e/2\pi T)^{1/2} e^{m_e(v_x - U_x)^2/2T}$  and  $f_y = (m_e/2\pi T)^{1/2} e^{m_e(v_y - U_y)^2/2T}$ , and substitute f into the steady 6D Liouville equation in phase space (x, v) (Zank et al. 2014),

$$\mathbf{v} \cdot \frac{\partial f}{\partial \mathbf{x}} + \frac{\mathbf{F}}{m_e} \frac{\partial f}{\partial \mathbf{v}} + f \frac{\partial}{\partial \mathbf{v}} \left( \frac{\mathbf{F}}{m_e} \right) = 0, \tag{6}$$

and integrate over  $v_x$  and  $v_y$ , to obtain

$$U_{d} \cdot \frac{\partial f_{z}}{\partial x_{in}} + \frac{F_{z}}{m_{e}} \frac{\partial f_{z}}{\partial v_{z}} + f_{z} \frac{\partial}{\partial v_{z}} \left( \frac{F_{z}}{m_{e}} \right) = 0. \tag{7}$$

where  $U_d = U_x \hat{x} + U_y \hat{y}$  is the drift in the x-y plane. The diffusion time  $\tau_d$  is the time that the electrons stay in the vortices and are accelerated, and it is longer than the lifetime of the localized induced  $E_z$ . We assume the spatial scale of the vortices is R and the average flow velocity is  $U_d$ , and

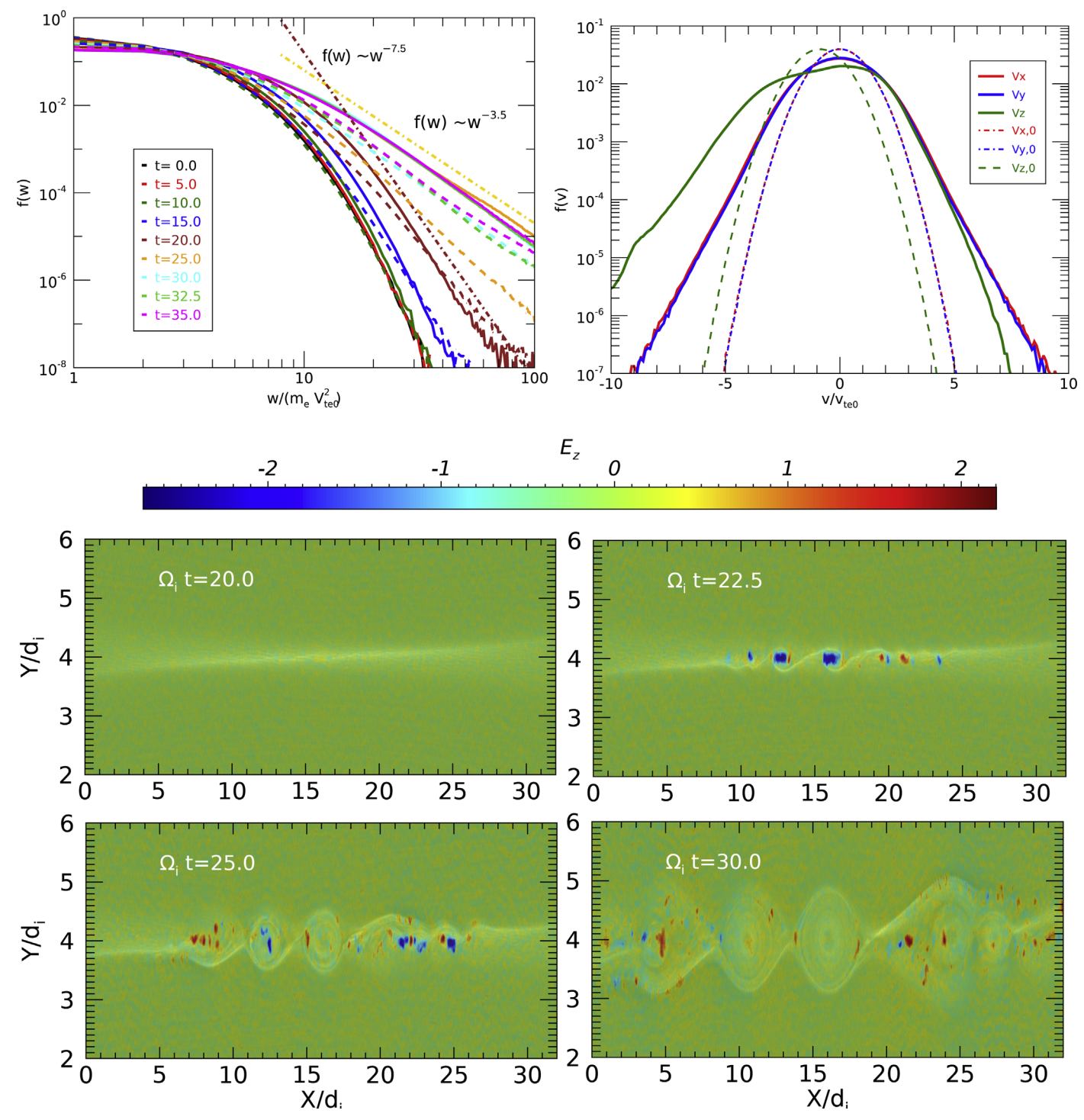


Figure 6. Top right: the electron energy spectra at different times during magnetic reconnection. The solid lines are f(W) measured in the vortices, and the dashed lines represent f(W) measured in the primary magnetic island of reconnection. f(W) is the electron number in each energy bin normalized by the total electron number. Top left: the electron velocity component distributions  $f(v_{ex})$ ,  $f(v_{ey})$  and  $f(v_{ez})$  at  $\Omega_i t = 0$  and 35, illustrating the initial and final stage of the reconnection, respectively. Bottom: the inductive  $E_z$  produced by the expanding vortices at  $\Omega_i t = 20$ , 22.5, 25 and 30.

 $\tau_d = R/U_d$ . We average Equation (7) over R, and using

 $\left\langle U_d \cdot \frac{\partial f_z}{\partial x_{ip}} \right\rangle \sim \frac{\bar{f}_z U_d}{R} = \frac{\bar{f}_z}{\tau_d}, \left\langle f_z(x_{ip}, v_z) \right\rangle = \bar{f}_z(v_z),$ 

we obtain

$$\frac{\bar{f}_z}{\tau_d} + \frac{\cos^2 \theta}{2\tau_g} v_z \frac{\partial \bar{f}_z}{\partial v_z} + \bar{f}_z \frac{\partial}{\partial v_z} \left( \frac{\cos^2 \theta}{2\tau_g} v_z \right) = 0.$$
 (8)

The solution is

$$\bar{f}_z(v_z) \propto v_z^{-\left(1 + \frac{2\tau_g}{\cos^2\theta\tau_d}\right)}$$
 (9)

The energy distribution function is thus

$$\bar{f}_z(W_z) \propto W_z^{-\left(1 + \frac{2\tau_g}{\cos^2\theta \tau_d}\right)/2}$$
 (10)

 $B_{ip}$  varies from 0 to  $B_0$ , thus we need to use the mean value of  $\langle \cos^2 \theta \rangle$ . We rewrite  $\cos^2 \theta = B_{ip}^2/a^2B_0^2$ , where  $a = B_z/B_0$ ,  $-1 \leqslant B_{ip}/B_0 \leqslant 1$ , thus  $\langle \cos^2 \theta \rangle = 1/2a^2$ . In our simulation  $a \sim 2.5$ , therefore,  $\langle \cos^2 \theta \rangle \approx 1/13$ . As  $U_d$  is caused by the drift  $U_d \sim E_z c/B_{ip}$  and  $E_z \sim DB_{ip}/(c\tau_g)$ , we have  $U_d \sim D/\tau_g$ , where D is the characteristic spatial scale of the inductive electric field, and  $\tau_d \sim R\tau_g/D$ . Thus  $2\tau_g/(\langle \cos^2 \theta \rangle \tau_d) \sim 4a^2D/R$ . We rewrite Equations (9) and (10):

$$\bar{f}_z(v_z) \propto v_z^{-(1+4a^2\frac{D}{R})},$$
 (11)

and

$$\bar{f}_z(W_z) \propto W_z^{-\left(1+4a^2\frac{D}{R}\right)/2}$$
 (12)

At the saturation of EKHI,  $D \sim R/4$  and then  $4a^2D/R \sim 6$ , so we have

$$\bar{f}_z(v_z) \propto v_z^{-7}; \bar{f}_z(w_z) \propto W_z^{-3.5},$$

which is consistent with the power-law index at the saturation of EKHI shown in Figure 6.

# 4. Conclusions

Past simulations of electron acceleration by tearing instability induced multi-islands suggested an "injection problem," such that in mildly relativistic MR regime multi-island acceleration cannot produce the observed power-law energy/ velocity spectra. In this paper, we have examined a new acceleration scenario in which electrons are accelerated by the stochastic electric field induced by the expansion of vortices generated by EKHI during MR with a strong guide field. The generation of vortices twists and entangles magnetic fields and drives localized MR and associated inductive electric fields that inversely transfer the energy from electron inertial to ion inertial scales. The randomly distributed inductive electric field within the vortices produces a suprathermal electron tail whose energy spectrum is a power law  $f(W) \propto W^{-\alpha}$ , where the index is determined by the expansion timescale of vortices  $\tau_g$  and the electron drift time in a vortex  $\tau_d$ , i.e.,  $\alpha = (1 + 2\tau_g/(\langle \cos^2 \theta \rangle \tau_d))/2$ , where  $\langle \cos \theta \rangle = 1/2a^2$ , where drift  $a = B_g/B_0$ . Using Farady's law and  $E \times B$ , an expression of the mean power-law index  $\alpha = (1 + 4a^2D/R)$  is obtained, where D is the characteristic spatial scale of the inductive electric field and R is the characteristic spatial scale of the vortex at the saturation of EKHI. The analytic expression is consistent with the simulation results. In the process, the electrons experience two phases of acceleration. At the linear stage of EKHI, the electrons achieve a power-law energy spectrum with  $\alpha \sim 7.5$ , and at the nonlinear stage,  $\alpha$  quickly reaches 3.5, which is close to the index of highly energetic electrons observed in solar flares (Benz 2017) and the superhalo electrons discovered in the solar wind (Wang et al. 2012).

Comparing with tearing instability induced multi-island acceleration, multivortices acceleration is more efficient, because the growth rate of the EKHI is much greater than that of the tearing instability. In multi-island MR, particles absorb magnetic energy as the particles circulate inside the island where the first and second adiabatic invariants hold. An inductive electric field is also generated in multi-island MR, but it is localized and weak and as a result, the particle acceleration is not continuous and therefore less efficient (Du et al. 2018). In contrast, magnetic vortices accelerate particles by volumefilling stochastic inductive electric fields which are much stronger than those generated by island contraction. The main difference between the two is the mechanism that produces the power-law electron energy spectrum. In multi-island MR, particles are randomized by the repetitive acceleration and scattering between numerous islands. This process is rather slow, as the timescale of particle confinement in one island in mildly relativistic MR is nearly comparable to the MR timescale (Drake et al. 2006). Multivortices acceleration, on the other hand, randomize particles efficiently by the inductive electric fields generated by turbulent magnetic fields in vortices, and a power law develops during the time of acceleration inside the vortices. The timescale of the acceleration is  $\sim \Omega_i^{-1}$ , which is about one to two orders of magnitude shorter than that of the multi-island reconnection. In our simulation, the fraction of electrons accelerated above 10 times the initial electron thermal energy is  $\sim 10\%$  in the vortices, while this fraction is only  $\sim$ 4% in the reconnection magnetic island.

Solar flares produces  $10^{38}$  energetic electrons in about  $10^3$  s (Benz 2017). Assuming the electron density is  $\sim 10^9$  cm<sup>-3</sup> =  $10^{24}$  km<sup>-3</sup>, and the current sheet spatial dimensions are  $\sim 10^4 \times 10^4 \times 0.01$  km<sup>3</sup>, then the number of electrons in the acceleration region is  $\sim 10^{24} \times 10^4 \times 10^4 \times 0.01 = 10^{32}$ . The timescale of multivorticles acceleration is  $\sim \Omega_i^{-1}$ , which is about  $10^{-4}$  s in the corona. A  $10^3$  s flare is thus  $\sim 10^7$  times the acceleration time in the vortices, and the number of total accelerated electrons by multivortices can be estimated as  $10^{32} \times 0.1 \times 10^7 = 10^{38}$  (we have used the result from our simulation that 10% of the electrons in the acceleration region are accelerated above 10 times their thermal energy), which is consistent with observations. During the flares the thermal electrons are supplied by return currents and the background electrons.

Stochastic electric field acceleration may explain the softer power-law energy spectrum of energetic electrons produced in solar flares and solar wind, and provide an alternative to multi-island acceleration that does not suffer from the "injection problem". We also carried out 2D PIC simulations with the same parameters. We found that a 2D EKHI is triggered and a similar power-law energy spectrum is obtained. In the future, we will explore large 3D PIC simulations with a larger *z* and study how the plasma heating produced by other possible instabilities affects the power-law spectrum.

H.C. is very grateful to Dr. Y. Yang for his help in analyzing the simulations and providing critical comments on the manuscript. H.C. is grateful for the critical discussions with Drs. D. Escande and P.H. Diamond at the "10th Festival de Théorie" held in Aix-en-Provence, France, 2019, in particular, Dr. Escande's careful reading of this manuscript. H.C. would also like to thank Dr. A.O. Benz for his critical comments and

discussions. The authors thank the anonymous referee for the comments that helped to improve this manuscript. The authors acknowledge the partial support of an NSF EPSCoR RII-Track-1 Cooperative Agreement OIA-1655280. H.C. acknowledges support by NASA Heliophysics Career award No. 80NSSC19K1106 and HSR program No. NNX17AI19G, and G.P.Z. acknowledges partial support from an NSF/DOE Partnership in Basic Plasma Science and Engineering via NSF grant PHY-1707247. The simulations were supported by the NASA High-End Computing (HEC) Program through the NASA Advanced Supercomputing (NAS) Division at Ames Research Center.

## **ORCID iDs**

H. Che https://orcid.org/0000-0002-2240-6728 G. P. Zank https://orcid.org/0000-0002-4642-6192

### References

```
Baker, D. N., Pulkkinen, T. I., Angelopoulos, V., Baumjohann, W., & McPherron, R. L. 1996, JGRA, 101, 12975
Benz, A. O. 2017, LRSP, 14, 2
Blandford, R., Simeon, P., & Yuan, Y. 2014, NuPhS, 256, 9
Blandford, R., Yuan, Y., Hoshino, M., & Sironi, L. 2017, SSRv, 207, 291
Bühler, R., & Blandford, R. 2014, RPPh, 77, 066901
Che, H., & Zank, G. P. 2019, JPhCS, 1332, 012003
Dahlin, J. T., Drake, J. F., & Swisdak, M. 2014, PhPl, 21, 092304
Dahlin, J. T., Drake, J. F., & Swisdak, M. 2017, PhPl, 24, 092110
Daughton, W., Roytershteyn, V., Karimabadi, H., et al. 2011, NatPh, 7, 539
Drake, J. F., Swisdak, M., Che, H., & Shay, M. A. 2006, Natur, 443, 553
Drake, J. F., Swisdak, M., & Fermo, R. 2013, ApJL, 763, L5
Du, S., Zank, G. P., Guo, F., Li, X., & Stanier, A. 2018, JPhCS, 1100, 012009
```

```
Galeev, A. A., Kuznetsova, M. M., & Zelenyi, L. M. 1986, SSRv, 44, 1
Gloeckler, G., Fisk, L. A., Zurbuchen, T. H., & Schwadron, N. A. 2000, in
   AIP. Conf. 528, Acceleration and Transport of Energetic Particles Observed
   in the Heliosphere, ed. R. A. Mewaldt (Melville, NY: AIP), 221
Gosling, J. T., & Phan, T. D. 2013, ApJL, 763, L39
Guo, F., Li, H., Daughton, W., & Liu, Y.-H. 2014, PhRvL, 113, 155005
Guo, F., Li, X., Li, H., et al. 2016, ApJL, 818, L9
Huang, C., Lu, Q., Guo, F., et al. 2015, GeoRL, 42, 7282
Huang, C., Lu, Q., Wang, R., et al. 2017, ApJ, 835, 245
Kiplinger, A. L., Dennis, B. R., Frost, K. J., & Orwig, L. E. 1984, ApJL,
   287, L105
Kliem, B. 1994, ApJS, 90, 719
Kouveliotou, C., Wijers, R. A. M. J., & Woosley, S. 2012, Gamma-ray Bursts
   (Cambridge: Cambridge Univ. Press)
le Roux, J. A., Zank, G. P., & Khabarova, O. V. 2018, ApJ, 864, 158
le Roux, J. A., Zank, G. P., Webb, G. M., & Khabarova, O. 2015, ApJ,
   801, 112
Lin, R. P. 2011, SSRv, 159, 421
Muñoz, P. A., & Büchner, J. 2018, ApJ, 864, 92
Oka, M., Birn, J., Battaglia, M., et al. 2018, SSRv, 214, 82
Oka, M., Phan, T.-D., Krucker, S., Fujimoto, M., & Shinohara, I. 2010, ApJ,
   714, 915
Sironi, L., & Spitkovsky, A. 2014, ApJL, 783, L21
Stone, E. C., Cummings, A. C., McDonald, F. B., et al. 2005, Sci, 309, 2017
Tavani, M., Bulgarelli, A., Vittorini, V., et al. 2011, Sci, 331, 736
Vech, D., Mallet, A., Klein, K. G., & Kasper, J. C. 2018, ApJL, 855, L27
Wang, L., Lin, R. P., Salem, C., et al. 2012, ApJL, 753, L23
Werner, G. R., Uzdensky, D. A., Cerutti, B., Nalewajko, K., &
   Begelman, M. C. 2016, ApJL, 816, L8
Zank, G. P., Hunana, P., Mostafavi, P., et al. 2015, ApJ, 814, 137
Zank, G. P., le Roux, J. A., Webb, G. M., Dosch, A., & Khabarova, O. 2014,
   ApJ, 797, 28
Zelenyi, L. M., Artemyev, A. V., Malova, K. V., Petrukovich, A. A., &
   Nakamura, R. 2010, PhyU, 53, 933
```

Dungey, J. W. 1961, PhRvL, 6, 47